A Kalman Filter Analysis of Sea Level Height in the Tropical Pacific

ROBERT N. MILLER

College of Oceanography, Oregon State University, Corvallis, Oregon

MARK A. CANE

Lamont-Doherty Geological Observatory of Columbia University, Palisades, New York

(Manuscript received 1 August 1988, in final form 27 December 1988)

ABSTRACT

The Kalman filter is implemented and tested for a simple model of sea level anomalies in the tropical Pacific, using tide gauge data from six selected island stations to update the model. The Kalman filter requires detailed statistical assumptions about the errors in the model and the data. In this study, it is assumed that the model errors are dominated by the errors in the wind stress analysis. The error model is a simple covariance function with parameters fit from the observed differences between the tide gauge data and the model output. The fitted parameters are consistent with independent estimates of the errors in the wind stress analysis. The calibrated error model is used in a Kalman filtering scheme to generate monthly sea level height anomaly maps for the tropical Pacific. The filtered maps, i. e., those which result from data assimilation, exhibit fine structure that is absent from the unfiltered model output, even in regions removed from the data insertion points. Error estimates, an important byproduct of the scheme, suggest that the filter reduces the error in the equatorial wave guide by about 1 cm. The few independent verification points available are consistent with this estimate. Given that only six data points participate in the data assimilation, the results are encouraging, but it is obvious that model errors cannot be substantially reduced without more data.

1. Introduction

In the work reported here, a Kalman filter is used to assimilate data into a wind-driven numerical model for the equatorial Pacific in order to produce monthly mean sea level maps for the period 1978–83. To our knowledge, this is the first application of a true Kalman filter to a real oceanographic problem. Given the current high level of enthusiasm for both "data assimilation" and "sea level data" among oceanographers, any introductory justification for considering these broad topics is superfluous. We therefore present only a brief discussion of our particular choices of problem and methodology to frame the issues at the core of this study.

Primarily through the collection and analysis of tide gauge data by Wyrtki (see especially 1975, 1979), the study of tropical Pacific sea level data has advanced our understanding of both annual and interannual changes in the tropical ocean. Indeed, Cane (1986) has argued that Wyrtki's shift of attention from sea surface temperature to sea level variations was the crucial insight leading to a dynamical theory for El Niño and the Southern Oscillation (ENSO). Current theory, while characterizing ENSO as a cycle of the coupled ocean–atmosphere system, assigns a pivotal role to variations in tropical sea level (more precisely, to its near equivalents, dynamic topography or heat content). Dynamical prediction efforts (Cane et al. 1986), which are based on this view of the ENSO cycle, have an essential requirement for fields of tropical Pacific sea level as initial conditions.

Maps of sea level (or equivalent) have been produced regularly from tide gauge station measurements (distributed monthly in the Climate Diagnostics Bulletin by the Climate Analysis Center/NMC/NOAA, Washington, D.C.; see also Wyrtki and Nakahara 1984), from XBT data (White et al. 1987), and from Geosat altimeter data (Cheney et al. 1987). The first two data sources provide only very sparse coverage, so much of the field must be created by an interpolation scheme. The last provides ample coverage, but may have errors which are large relative to the characteristic size of anomalies and is, in any case, too new to allow reliable definition of means and anomalies. For these reasons, it must still be regarded as experimental. Fields of sea level also may be created with a wind driven numerical model, which necessarily provides an estimate everywhere within the model domain. This approach is taken by Cane et al. (1986), who initialize their forecast runs with the ocean fields created by driving the ocean component of their coupled dynamical model with analyzed monthly mean wind fields derived from merchant

Corresponding author address: Dr. Robert N. Miller, College of Oceanography, Oregon State University, Corvallis, OR 97331.

ship observations (Goldenberg and O'Brien 1981). As discussed further below, the sparseness of the wind observations means that the accuracy of the analyzed fields is poor, and numerous studies (e.g., see McPhaden et al. 1988) have shown that the consequent errors in sea level can be comparable to all but the most extreme anomaly signals. In principle, the best field should result from a procedure which combines estimates from a model with in situ data. Work in this vein has been reported by Leetmaa and Ji (1989), who applied a relatively simple data assimilation scheme to a complex model, an ocean GCM.

Here we apply a sophisticated data assimilation methodology, the Kalman filter, to a 2 vertical mode, 5 meridional mode, linear wind-driven numerical model. There are numerous studies which support the contention that such a simple model is adequate to our purpose of hindcasting sea level in the equatorial waveguide.

The paper by Gill (1983) is an especially interesting heuristic precursor to the work reported here. He used a similar model to estimate sea level and surface current anomalies at Canton and Christmas Islands based on Kelvin and Rossby wave amplitudes estimated from data taken at the Galapagos. Gill did not calculate error statistics, but even if he had, direct comparison between that work and ours would be difficult.

Though in principle a more elaborate model should do a better job, we are aware of no evidence which establishes that this is now the case. Perhaps this merely reflects the paucity of evidence one way or the other; the only reported results of a GCM study for a long time series are those of Latif (1987). For present purposes, it is sufficient to argue that the linear dynamics of our model represent the dominant sea level response, and that its deficiencies in this regard are dwarfed by errors in the surface wind forcing. Consequently, we take the "model error" to be due entirely to wind error. However, in view of the empirical way that our model error is determined, the reader who disagrees with us is invited to attribute as much as he wishes of the model error to model shortcomings. Such a change in interpretation has only a small effect on our conclusions about our assimilation methodology.

In contrast to the simplicity of the physical model, the Kalman filter, widely used in engineering practice, is by some criteria a more sophisticated data assimilation procedure than any now in operational use in meteorology or oceanography. If certain conditions are met, it can be shown to yield an estimate of the present state of the system which is statistically optimal. In some respects, the sea level hindcasting problem is an ideal candidate for Kalman filtering. The evolution equations are predominantly linear. The errors result largely from errors in the forcing (and, if you like, model deficiencies), as opposed to the loss of predictability inherent in nonlinear dynamics. Application of the Kalman filter in the context of numerical weather prediction was first presented by Ghil (e.g., see Ghil et al. 1981).

Implementation of the Kalman filter requires that the covariances of the errors in the model and in the data be specified explicitly. Such detailed quantitative knowledge is not available; our ignorance permits only crude approximations. One of the goals of this study is to see if the filter retains any efficacy when subjected to assumptions that are not easily defensible in terms of the real world. Still, it bears repeating that every data assimilation scheme which is based upon minimization of an error functional involves error models of some sort. As an example, one might consider the strong constraint methods (Sasaki 1970), in which the analyzed field is a solution to the model equations, with the initial and boundary conditions chosen so that the resulting solution agrees most closely with observations. In such schemes the model error is assumed to vanish identically. This is a detailed, if trivial, error model. The Kalman filter can be implemented in strong constraint form. The need for explicit error statistics is often cited as a disadvantage of the Kalman filter; in fact, all statistically based data assimilation schemes require estimates of error statistics in some form.

The major disadvantage of the Kalman filter can be cost. In its most straightforward implementation, the cost of the Kalman filter increases quadratically with the number of state variables in the dynamical system. Applications to even as large a system as that studied here are rare. The computational burden here is easily managed, but it could be prohibitive in a high resolution model such as a GCM. A goal of our research is to find ways to implement the Kalman filter in such a context, perhaps in some approximate form, and the present application to a minimal model contributes to that goal in two ways: First, it provides an encouraging indication that the filter can be implemented readily and to good effect; second, as an illustrative example of the workings of the methodology on a practical problem in oceanography, it provides guidance for future work.

The physical model, the Kalman filter and the data are described in sections 2, 3 and 4 respectively. The parameterization of error statistics necessary for implementation of the Kalman filter is described in section 5. The model performance without data assimilation is described in section 6. Quantitative details of the testing and calibration of the error model are given in section 7. Section 8 describes the filtered results and section 9 contains discussion and summary.

2. The physical model

Our physical model, the linearized equations of motion on an equatorial beta plane with the long wave approximation, has been described in many places. Our notation is most like Cane (1984) and Cane and Sarachik (1981; hereafter CSII). In this model, the motion

is decomposed into vertical modes as in Cane (1984). The amplitude of each vertical mode satisfies the linearized shallow water equations on the beta plane, subject to long-wave approximations. Solutions obtained by classical separation of variables take the form

$$\begin{pmatrix} u_m \\ h_m \end{pmatrix} = \frac{a_{k,m}(x,t)}{2^{1/2}} \begin{pmatrix} \psi_0(y) \\ \psi_0(y) \end{pmatrix} + \sum_n^N \frac{r_{n,m}(x,t)}{2 \cdot 2^{1/2}} \begin{pmatrix} (n+1)^{-1/2}\psi_{n+1} - n^{-1/2}\psi_{n-1} \\ (n+1)^{-1/2}\psi_{n+1} + n^{-1/2}\psi_{n-1} \end{pmatrix}. \quad (1)$$

The subscript m denotes quantities associated with the mth baroclinic mode. In the above equation:

u_m the zonal velocity component
h_m the sea level height anomaly; the total sea level anomaly is $\sum_m h_m$
$a_{k,m}$ the amplitude of the Kelvin wave
$r_{n,m}$ the amplitude of the nth meridional mode Rossby wave
ψ_n the nth Hermite function (cf. CSII).

The a_k and r_n for the mth baroclinic mode are governed by the simple wave equations:

$$\frac{\partial a_k}{\partial t} + c_m \frac{\partial a_k}{\partial x} = \tau_k(x,t) \quad (2)$$

$$\frac{\partial r_n}{\partial t} - \frac{c_m}{2n+1} \frac{\partial r_n}{\partial x} = \tau_n(x,t) \quad (3)$$

subject to the boundary conditions

$$u = 0 \quad \text{at} \quad x = X_E \quad (4)$$

$$\int u dy = 0 \quad \text{at} \quad x = 0 \quad (5)$$

where $x = 0$ and $x = X_E$ are respectively the western and eastern boundaries of the ocean basin; τ_k and τ_n are calculated by projecting the zonal wind stress field on the meridional modes.

The model itself is implemented using the method of characteristics to solve (2) and (3) explicitly. Computation proceeds in three distinct steps. First the Kelvin wave amplitude a_k is calculated by explicitly solving (2) as an ordinary differential equation along the characteristics $x = c_m t + x_0$ in the x–t plane. Physically this amounts to simulating the eastward propagation of the forced Kelvin wave. This calculation only involves those points which are not influenced by the western boundary, i.e., those points which lie a distance of at least $c_m \Delta t$ east of the western boundary. The amplitude of the Kelvin wave at the eastern boundary determines the amplitude of the Rossby waves there through the boundary condition (4). In order to satisfy (4) we must have (cf. CSII)

$$r_1(X_E, t) = 2a_k(X_E, t)$$

and, in general:

$$r_{n+1}(X_E, t) = \left(\frac{n+1}{n}\right)^{1/2} r_{n-1}(X_E, t)$$

for even $n > 0$; these are the symmetric modes which interact with the Kelvin waves. The antisymmetric modes have zero amplitudes at the eastern boundary.

Since we must truncate the series in (1) at some finite N, (4) will not be satisfied exactly. This introduces some dissipation into the numerical scheme: neglect of the higher modes means energy is lost at the eastern boundary and mass is not conserved there. Energy is also lost at the western boundary. This follows from the derivation of (5) (cf. CSII). It has been widely noted (cf. CSII) that the Hermite series converges very slowly, and does not efficiently represent the solutions to the underlying equations outside a narrow band of latitudes near the equator.

Once the r_n are known on the eastern boundary, (3) can be solved for the entire domain. The result of this step yields the values of r_n on the western boundary, and this, in turn allows the values of a_k to be calculated for the western boundary by (5). Equation (2) is then solved as a signaling problem for the values of a_k near the western boundary. As noted above, (2) and (3) are treated as ordinary differential equations in the characteristic plane. Linear interpolation is used to estimate initial values and the quadrature is done by the midpoint rule. We use common Pacific values (cf. Cane 1984) for physical parameters in the model, i.e., wave speeds of 2.91 and 1.78 m s^{-1} and length scales of 357 and 279 km for the first and second baroclinic modes, respectively.

To combine the dynamical model with the Kalman filter we take a state space approach. For each of the two vertical modes, we calculate five meridional Rossby mode amplitudes and a Kelvin wave amplitude at each longitude. Our model extends from 125°E to 80°W in 5° intervals. Thus we have 12 values at each of the 32 gridpoints in the model domain for a total of 384 values at each time. These values are the components of the state vector $\mathbf{w}$ which completely specifies the model. Our numerical scheme, then, is a method which, given a state vector and a wind field, can predict the state vector at the next time step, 10 days hence in this case.

Within this framework, we may write our numerical model as

$$\mathbf{w}_{k+1}^f = \mathbf{L}\mathbf{w}_k^a + \tau_k,$$

where the subscripts denote time step, superscript f denotes "forecast" and superscript a denotes "analysis", our best guess at the state vector at time t_k.

The vector τ is the forcing. The matrix $\mathbf{L}$ represents our numerical scheme for the left hand sides of (2) and (3).

3. The data assimilation scheme: the Kalman filter

We assume that the model system differs from the true system by random noise, i.e., the underlying dynamics obey:

$$\mathbf{w}^t_{k+1} = \mathbf{L}\mathbf{w}_k^t + \tau_k + \mathbf{b}_k,$$

where the quantities with the superscript "t" represent the true system and $\mathbf{b}_k$ is a random variable uncorrelated from time step to time step:

$$\langle \mathbf{b}_j \mathbf{b}_k^{\mathrm{T}} \rangle = \mathbf{Q}_k \delta_{jk},$$

where each $\mathbf{Q}_k$ is a positive semidefinite matrix which we shall refer to as the "system noise covariance". The superscript "T" denotes the transpose.

The only information we have from the true system comes to us in the form of observed data. When data become available, we use them to form a correction to the forecast. The procedure we use to form this correction is the Kalman filter. The basic formalism which follows is essentially identical to that first introduced by Ghil (e.g., see Ghil et al. 1981), who first developed the Kalman filter in the context of numerical weather prediction.

Ghil's formulation was later applied to a prototype problem in numerical ocean modeling by Miller (1986).

Assume that at a given time there are observations $\mathbf{w}^0_{k+1}$ available which are related to the true state vector $\mathbf{w}^t_{k+1}$ by:

$$\mathbf{w}^0_{k+1} = \mathbf{H}_{k+1}\mathbf{w}^t_{k+1} + \mathbf{b}^0_{k+1}, \tag{6}$$

where $\mathbf{b}^0_{k+1}$ is the observation error, which is assumed to be a white sequence with zero mean and covariance given by $\langle \mathbf{b}^0_{k+1}\mathbf{b}^{0\mathrm{T}}_{k+1} \rangle = \mathbf{R}_{k+1}$. Here $\mathbf{H}_k$ is the linear transformation which relates the state variables, in our case the Kelvin and Rossby wave amplitudes, to the observed quantities, i.e., the sea level heights at time t_k. The actual coefficients in $\mathbf{H}_k$ are determined by (1). In order to form the correction we must estimate the forecast error covariance

$$\mathbf{P}^f_{k+1} = \langle (\mathbf{w}^t_{k+1} - \mathbf{w}^f_{k+1})(\mathbf{w}^t_{k+1} - \mathbf{w}^f_{k+1})^{\mathrm{T}} \rangle.$$

If the error covariance of the analyzed field at time t_k is

$$\langle (\mathbf{w}_k^t - \mathbf{w}_k^a)(\mathbf{w}_k^t - \mathbf{w}_k^a)^{\mathrm{T}} \rangle = \mathbf{P}_k^a,$$

we may calculate

$$\mathbf{P}^f_{k+1} = \mathbf{L}\mathbf{P}_k^a\mathbf{L}^{\mathrm{T}} + \mathbf{Q}_{k+1}. \tag{7}$$

The updated state vector, the analysis, is taken to be a linear combination of the forecast and the observations. We write

$$\mathbf{w}^a_{k+1} = \mathbf{w}^f_{k+1} + \mathbf{K}_{k+1}(\mathbf{w}^0_{k+1} - \mathbf{H}_{k+1}\mathbf{w}^f_{k+1}),$$

where $\mathbf{K}_{k+1}$ is the Kalman gain matrix:

$$\mathbf{K}_{k+1} = \mathbf{P}^f_{k+1}\mathbf{H}^{\mathrm{T}}_{k+1}(\mathbf{H}_{k+1}\mathbf{P}^f_{k+1}\mathbf{H}^{\mathrm{T}}_{k+1} + \mathbf{R}_{k+1})^{-1}.$$

The error covariance of the updated field is given by

$$\mathbf{P}^a_{k+1} = (\mathbf{I} - \mathbf{K}_{k+1}\mathbf{H}_{k+1})\mathbf{P}^f_{k+1}.$$

The most expensive step is (7), the covariance update, which requires two prediction steps per state variable. It is not prohibitively expensive. A typical run with our 384 state variable model takes under two hours on the Masscomp 5600 to simulate six years with 10-day time steps. Further improvement is possible since no effort has been made to optimize our code.

In order to use this scheme, we must estimate $\mathbf{Q}$ and $\mathbf{R}$, the statistics of errors in the model and in the data. Here $\mathbf{R}$ may be estimated by consideration of the instruments and the manner of processing the data. Estimates of $\mathbf{Q}$ must be based upon assumptions about the physical and computational errors in the model. Such assumptions are always problematical. Our estimates of $\mathbf{Q}$ are empirically based and checked a posteriori for consistency; details are given in sections 5 and 7. Another approach would be to use an adaptive algorithm to estimate $\mathbf{Q}$ and $\mathbf{R}$ as in Dee et al. (1985).

4. The data

Our model requires two types of data: wind forcing data and sea level height for assimilation and verification.

a. *Wind data*

The wind data we use come from the FSU monthly pseudostress analysis (Goldenberg and O'Brien 1981). This is a subjective analysis based on ship observations, and little is known about its error characteristics. We do, however, have some basis for inference of error statistics based on comparison of different wind products. Halpern and Harrison (1982) carried out a one month study comparing wind products. They estimated the error amplitude to be about 2 m s^{-1}. Chelton and O'Brien (1982) compared SEASAT scatterometer winds with the FSU analysis. This work suggests highly spatially inhomogeneous wind stress error fields with an error magnitude consistent with the results of Halpern and Harrison.

b. *Sea level data*

Data were taken from tide gauges at various islands in the Pacific (Wyrtki et al. 1988). The locations of these islands are shown in Fig. 1. The raw data consist of monthly means with tides removed. We further process the data by removing the averages for each month to yield the monthly mean anomalies. These stations were chosen for two fundamental reasons: first, they are near the equator where the model is expected to do its best, and second, these six stations provide the longest overlapping time series. Because of the length

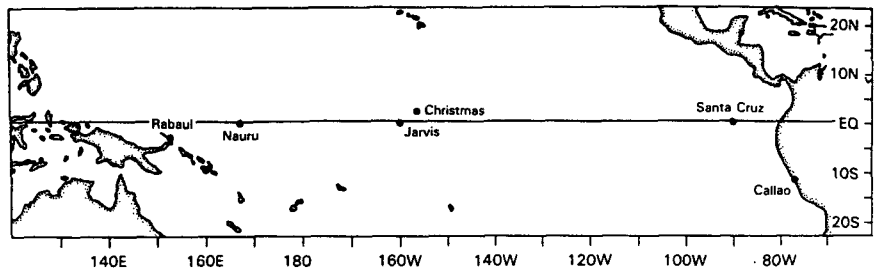

FIG. 1. The model domain, showing locations of tide gauges from which data are drawn for assimilation.

of the records, data from these locations raise the fewest questions about reliably removing the monthly means.

The tide gauge data can be considered accurate within 3 cm (K. Wyrtki, personal communication). The actual accuracy of reading the instrument is about 2 cm for the monthly average. In addition, the tide gauge is a point measurement, while the sea level predicted by the model is actually an average over some region several degrees in extent.

The locations of the tide gauges shown in Fig. 1 can be seen to cluster into three rough groups: Rabaul and Nauru in the west; Jarvis and Christmas in the central Pacific and Callao and Santa Cruz in the east. Some specific features should be noted. The record at Nauru contains rather strong local wind events that are the result of local geometry and should not be assimilated into the model. Callao at 12°S would seem to be near the southern edge of the waveguide, but at this level of approximation, the sea level is constant along the entire eastern boundary (cf. CSII). Intuitively, given the scale assumptions in the model, this is reasonable because any slope of the sea surface would result in a geostrophically balanced flow into the solid boundary. Physically, this amounts to the assumption that the time required for the coastal Kelvin wave to communicate meridional pressure differences is short compared to any time scale in the model. In practice, tide gauge readings from coastal stations differ significantly, partly due to the lack of precision of this assumption and partly due to local effects such as topography or local variation in the longshore winds.

5. The model error

a. *Parameterization of wind error statistics*

Our basic assumptions in constructing the system noise field are: (i) the dominant source of model error is error in the wind stress, and (ii) the wind stress error is statistically homogeneous. In view of the large wind errors, assumption (i) is thought to be reasonable, despite the simplicity of the model. Assumption (ii) is not strictly defensible (cf. Chelton and O'Brien 1982), but it is a reasonable starting point in the absence of more detailed knowledge of the structure of the wind stress error field. We shall see that our simple wind stress error model is adequate to establish bounds on the overall influence of error amplitude and scale upon forecast errors. We leave more elaborate realistic error models for future work.

Let the wind stress error at month j be given by $e_j(x, y)$. Assume

$$\langle e_j(x_1, y_1)e_k(x_0, y_0)\rangle = \delta_{jk}A \exp[-(x_1 - x_0)^2/L_x^2 - (y_1 - y_0)^2/L_y^2]. \quad (8)$$

This is a three-parameter model: error amplitude A and scales L_x and L_y. The assumption of serial independence is certainly questionable, but long-term biases aside, it is plausible that the errors in these subjective analyses may not be highly correlated from month to month. We also assume that the wind *stress* anomaly error (rather than the *wind* error) has Gaussian distribution with zero mean.

Since the model functions by decomposing the wind forcing into meridional modes, the wind stress error must be similarly decomposed. The projection of the zonal wind stress on the jth meridional mode is given by

$$\tau^{(j)}(x) = \int_{-\infty}^{\infty} w^{(j)}(y)\tau(x, y)dy, \quad (9)$$

where j is the index of the meridional mode ($j = -1$ is the Kelvin wave), τ is the zonal wind stress, and $w^{(j)}(y)$ is the weighting function in the projection. Since our model is linear, the error in forcing of the jth mode at the kth time step is given by

$$e_k{}^j(x) = \int_{-\infty}^{\infty} e_k(x, y)w^j(y)dy$$

(here superscripts denote mode and subscripts denote time, consistent with previous notation). Therefore,

$$e_k{}^j(x_0)e_m{}^l(x_1) = \int_{-\infty}^{\infty} e_k(x_0, y)w^j(y)dy \int_{-\infty}^{\infty} e_m(x_1, z)w^l(z)dz$$

$$= \int_{-\infty}^{\infty}\int_{-\infty}^{\infty} e_k(x_0, y)e_m(x_1, z)w^j(y)w^l(z)dydz.$$

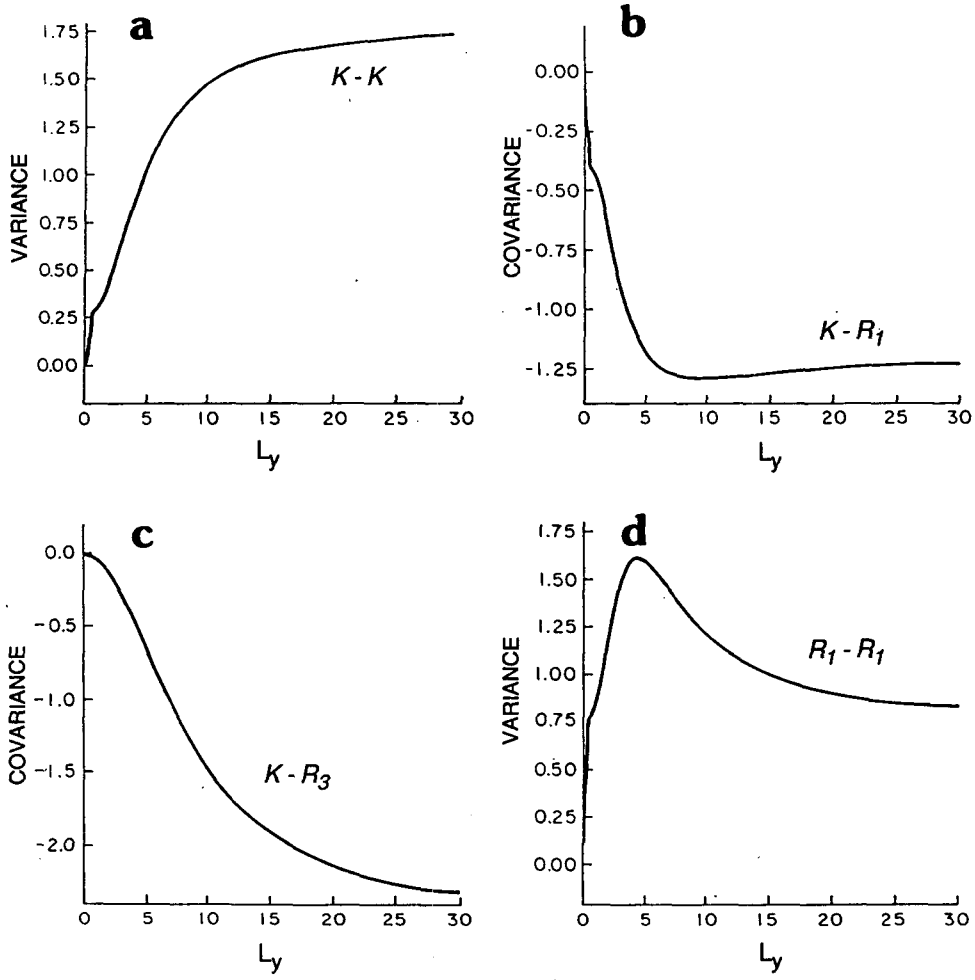

FIG. 2. Covariance among errors in meridional mode response due to errors in wind forcing as a function of the assumed correlation scale of the wind stress error. Here the abscissa is the meridional correlation length in degrees. The ordinate is the value of $\int_{-\infty}^{\infty}\int_{-\infty}^{\infty} \exp[-(y-z)^2/L_y^2]w^j(y)w^l(z)dydz$. The indices j and l denote the meridional modes; -1 denotes the Kelvin wave. (a) Variance of error in Kelvin wave forcing. (b) Covariance of error in Kelvin wave forcing and error in first meridional mode Rossby wave forcing. (c) Kelvin wave and third mode Rossby wave. (d) Variance of first mode Rossby wave forcing. (e) First Rossby wave and third Rossby wave. (f) Variance of second Rossby mode. (g) Variance of third Rossby mode. Covariance between the second Rossby mode and the other waves pictured here vanish identically by symmetry.

Taking expected values:

$$\langle e_k{}^j(x_0)e_m{}^l(x_1)\rangle$$

$$= \int_{-\infty}^{\infty}\int_{-\infty}^{\infty} \langle e_k(x_0, y)e_m(x_1, z)\rangle w^j(y)w^l(z)dydz$$

$$= \delta_{km}A \exp[-(x_1 - x_0)^2/L_x^2]$$

$$\times \int_{-\infty}^{\infty}\int_{-\infty}^{\infty} \exp[-(y-z)^2/L_y^2]w^j(y)w^l(z)dydz.$$

The double integral can be evaluated by numerical quadrature. The results as a function of L_y for the error covariance among the Kelvin wave and the first three meridional Rossby wave modes for the first baroclinic mode are shown in Fig. 2. These quadratures were performed numerically on a 2° grid, which is the resolution of the wind dataset. This is inaccurate for small L_y, but it is faithful to the way wind forcing enters the model. Asymptotic values for large L_y can be estimated by noting that as $L \to \infty$, the Gaussian error covariance function approaches 1 over most of the region in which the weighting functions differ significantly from zero, so the asymptotic limits may be calculated by simply integrating the weighting functions. As Fig. 2 shows, dependence of the total system noise covariance upon the meridional covariance scale L_y is complicated. The effect of varying L_y upon the covariance matrix which results from the given system noise will be investigated in section 7.

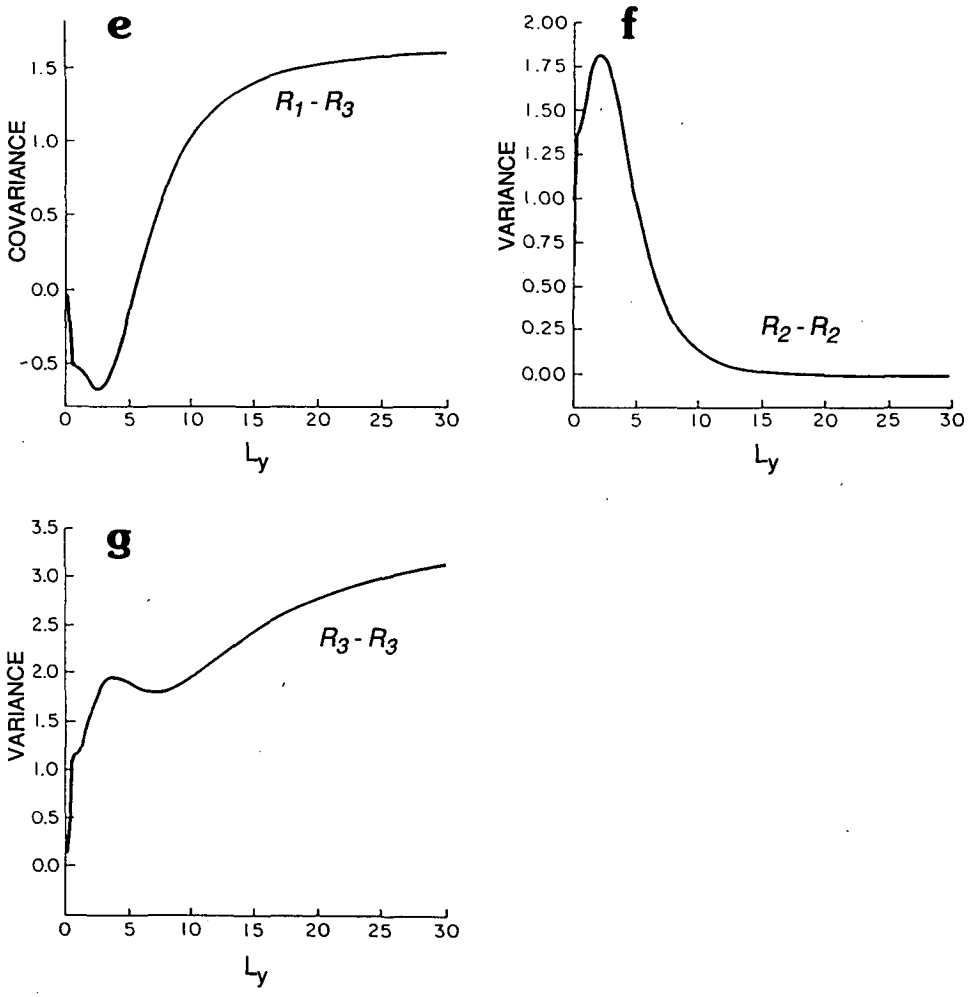

FIG. 2. (*Continued*)

Though our statistical model relates solely to wind stress as opposed to wind speed, we have found it helpful to write down a systematic if approximate relation between the two. This process of backing out the wind speed error from the wind stress error has aided us in placing our statistical wind stress error model in the context of the comparative wind speed studies of Halpern and Harrison (1982) and Chelton and O'Brien (1982).

The wind stress is given by

$$\frac{\tau}{\rho_w} = \frac{\rho_a}{\rho_w} C_D \mathbf{u}_a |\mathbf{u}_a|,$$

where C_D is the drag coefficient, $\mathbf{u}_a$ the surface wind velocity, and ρ_a, ρ_w are the densities of air and water respectively. We take the value of $(\rho_a/\rho_w)C_D$ to be 1.95×10^{-6} in our calculations.

Now let $u = u_0 + \Delta u$ where u_0 is the true wind velocity and Δu is the error. The error variance in the pseudostress $\mathbf{u}_a|\mathbf{u}_a|$ is

$$\langle (\mathbf{u}|\mathbf{u}| - \mathbf{u}_0|\mathbf{u}_0|)^2 \rangle = 4\sigma_\tau^2 \langle u_0^2 \rangle + 4\langle \Delta u^3 u_0 \rangle + \langle \Delta u^4 \rangle,$$

where we have assumed that the ensemble of wind speed errors have variance σ_τ^2 and are uncorrelated with the wind speed itself. We take $\langle u_0^2 \rangle = 25\ \mathrm{m^2\ s^{-2}}$, and estimate the other terms as if Δu were Gaussian. This leads to

$$\langle u_0 \Delta u^3 \rangle = 0; \quad \langle \Delta u^4 \rangle = 3\sigma_\tau^4,$$

so the pseudostress error variance becomes σ_τ^2 ($100\ \mathrm{m^2\ s^{-2}} + 3\sigma_\tau^2$). The value of σ_τ^2 is related in a straightforward manner to the parameter A, which is determined by a fitting procedure described in section 7.

b. Transfer of wind error into individual waves

The asymptotic error covariance of the individual waves can be investigated analytically in a straightforward fashion if we neglect interactions between the different wave modes. For the second and other even

mode Rossby waves, this neglect is entirely justified: since the boundary condition (4) implies that the amplitude of these waves vanishes at the eastern boundary, and symmetry considerations imply that these waves satisfy (5) identically, each of them is uncoupled from all other modes.

In the dissipation free case, the amplitude of the wave is governed by the partial differential equation:

$$u_t + cu_x = f(x, t).$$

(The phase speed c is negative for the Rossby waves.) Because the equation is linear, the error evolves by the same dynamics as the wave amplitude itself. For a single time step length Δt, for points more than $c\Delta t$ west of the eastern boundary, we have

$$u(x, t_0 + \Delta t) = u(x - c\Delta t, t_0) + \frac{1}{c}\int_{x-c\Delta t}^{x} f\left(z, t_0 + \Delta t + \frac{z-x}{c}\right)dz.$$

If we now consider u to be the error, its variance is given by

$$\langle u^2(x, t_0 + \Delta t)\rangle = \langle u^2(x - c\Delta t, t_0)\rangle + \frac{1}{c^2}\int_{x-c\Delta t}^{x}\int_{x-c\Delta t}^{x}\left\langle f\left(z', t_0 + \Delta t + \frac{z'-x}{c}\right) \times f\left(z, t_0 + \Delta t + \frac{z-x}{c}\right)\right\rangle dz'dz,$$

under the assumption that the modal amplitude error $u(x_0, t_0)$ is not correlated with the wind forcing error $f(x_1, t_1)$ for $t_1 \geq t_0$.

We now make the assumption that

$$\langle f(x_0, t_0)f(x_1, t_1)\rangle = (\sigma^2/\Delta t^2)e^{-(x_1-x_0)^2/L_x^2}$$

for t_0 and t_1 in the same month

$$= 0 \quad \text{for } t_0 \text{ and } t_1 \text{ in different months;}$$

recall that we have monthly data. (Note σ^2 has the dimensions of u^2.) In our simulations, time steps never bridge across months, so the integral becomes

$$\frac{\sigma^2}{\Delta t^2}\int_{x-c\Delta t}^{x}\int_{x-c\Delta t}^{x} e^{-(z'-z)^2/L_x^2}dz'dz = \frac{L_x\sigma^2}{\Delta t^2}\int_{-\mu}^{0}\int_{-\mu}^{0} e^{-(z'-z)^2}dz'dz,$$

where $\mu = |c\Delta t|/L_x$. After a bit of algebra, the expression for the variance becomes

$$\langle u^2(x, t_0 + \Delta t)\rangle = \langle u^2(x - c\Delta t, t_0)\rangle + \frac{\sigma^2}{\mu}\int_{-\mu}^{\mu} e^{-s^2}ds - \frac{\sigma^2}{\mu^2}(1 - e^{-\mu^2}).$$

The equilibrium solution is reached when

$$\langle u^2(x, t_0)\rangle = \langle u^2(x, t_0 + \Delta t)\rangle = \langle u^2(x - c\Delta t, t_0)\rangle + \frac{\sigma^2}{\mu}\int_{-\mu}^{\mu} e^{-s^2}ds - \frac{\sigma^2}{\mu^2}(1 - e^{-\mu^2}).$$

Suppose the wave travels considerably less than a correlation length in a time step, i.e., $\mu \ll 1$. This limit is approached for the Rossby waves, though not for the Kelvin waves.

Then

$$\langle u^2(x, t_0)\rangle \approx \langle u^2(x - c\Delta t, t_0)\rangle + \sigma^2,$$

and the error variance is independent of the zonal correlation length and increases linearly to the west (recall that $c < 0$) at a rate which depends inversely on wave speed. In the parameter range of interest ($L_x \geq 10°$, $\Delta t = 10$ days and $c \approx -0.6$ m s^{-1}), the slope of $\langle u^2\rangle$ as a function of x is not strongly sensitive to L_x.

In the other extreme case in which the wave travels many correlation lengths each time step, i.e., $\mu \gg 1$, the expression for the variance becomes

$$\langle u^2(x, t_0)\rangle \approx \langle u^2(x - c\Delta t, t_0)\rangle + \frac{\sigma^2\pi^{1/2}}{\mu} + O(\mu^{-2}).$$

This case, in which the errors average out, is the basis for the intuition that the Kelvin wave errors do not grow rapidly towards the eastern end of the waveguide. Since μ is the number of correlation lengths traveled by the wave in a single time step, we may think of the wave as being subjected to roughly that number of independent random perturbations, each with mean zero. We therefore expect the variance to be inversely proportional to μ; compare this to the previous estimate in which the variance increases by σ^2 in each length $c\Delta t$, independent of L_x.

To complete the problem we must consider the region near the eastern boundary $x = X_E$. The wave arriving at $X_E - \Delta x$ at time $t_0 + \Delta t$ left the eastern boundary at time $t_0 + \tilde{t}$ where

$$\tilde{t} = \Delta t - \frac{\Delta x}{c}.$$

Integrating along the characteristic yields

$$u(X_E - \Delta x, t_0 + \Delta t) = \frac{1}{c}\int_{X_E}^{X_E-\Delta x} f\left(x, t_0 + \tilde{t} + \frac{x}{c}\right)dx.$$

The analysis used in the interior case yields

$$\langle u^2(X_E - \Delta x, t)\rangle = \frac{\Delta x}{\mu^2 L_x}\sigma^2\int_{-\Delta x/L_x}^{\Delta x/L_x} e^{-s^2}ds - \frac{\sigma^2}{\mu^2}(1 - e^{-(\Delta x/L_x)^2}).$$

6. Unfiltered results

The model as described in section 2 above was run for the six-year interval from January 1978 through December 1983, for initial comparison with the tide gauge data at the island stations shown in Fig. 1. Raw results of these tests are shown by the thin lines in Fig. 3. Gaps in some of the sea level records complicate the comparisons of model output with the data. Another complication arises at Nauru where, as noted in section 2, local weather conditions combined with the placement of the instrument give rise to large spikes in the sea level record which are highly localized in space and time, and do not represent valid data for comparison or assimilation. One such spike occurs in the record in 1979 as an anomaly of 19.8 cm, making it the largest positive anomaly in the record. That spike was subjectively removed from our quantitative comparisons, and is treated for our purposes as a gap.

All model runs were performed with two baroclinic modes and five meridional modes. Experiments were performed with as many as nine meridional modes. The additional modes rarely resulted in significant changes in the output and did not necessarily result in increased accuracy in those cases in which the difference was noticeable. The resolution of the wind data is too coarse to allow the amplitude of the higher meridional modes to be calculated accurately.

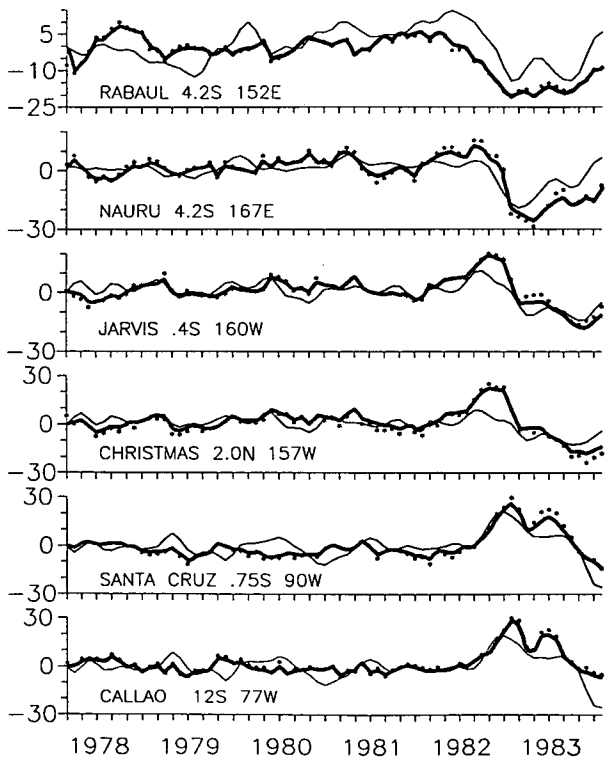

FIG. 3. Comparison of observation, raw model output and filtered model output at six selected tide gauge stations. Observed data points are marked with *; thin line: unfiltered model output; heavy line: filtered model output.

The dynamic topography output from this model is just that: dynamic. We include no source term in the mass equation. Once a mass anomaly is detected as a change in sea level, it will be advected around correctly, whatever its source.

Our formalism admits the addition of a thermal forcing term, but inclusion of such a term would involve the introduction of heat flux data, which are notoriously unreliable, and the cost in complication of our error model would be considerable. We therefore accept our inability to deal with steric effects. This is not as serious as it may seem. Assuming a thermal expansion coefficient of $2 \times 10^{-4}/°C$, a temperature anomaly of 1 °C over a depth of 50 m would be required for a change of 1 dynamic centimeter.

The unfiltered model underpredicted the 1982–83 ENSO event at every station except Rabaul. The model sea level anomaly was particularly weak at Christmas Island. There, the 1982–83 response is barely stronger than that of the non-ENSO season of 1980–81. We believe, but cannot prove, that this is due to an overly conservative estimate of anomalies in the wind products which necessarily bias regions of sparse data toward climatology.

Other possibilities are model deficiencies or an underestimate of the drag coefficient. Weighing against the former is the fact that ocean GCMs also understate the response; e.g., see Latif (1987).

7. Testing and calibration of the wind error model

We now describe the calibration of the wind error model (8) by estimating the values of the parameters A, L_x and L_y which are optimal in some sense. We begin by comparing the unfiltered model output with the tide gauge data over five years of a six-year run, leaving the first year for spinup. We use these comparisons to calculate covariance matrices. In the language of section 2, above, we estimate that

$$\langle (\mathbf{w}_j^0 - H\mathbf{u}_j{}^f)(\mathbf{w}_j^0 - H\mathbf{u}_j{}^f)^T \rangle = HPH^T + R. \quad (10)$$

Here, P without subscripts or superscripts represents the equilibrium value of the error covariance matrix of the forecast state vector. We then calculate the system noise matrix Q (constant in time for this error model) for a particular choice of parameters and use this Q in (7), iterated to convergence, to find the equilibrium value $\tilde{P}$. We then choose the parameter values resulting in estimates which agree most closely with the statistics (10) of the comparison between the model output and the data.

These statistical comparisons were not straightforward. We adopted a simple strategy to test the reliability of the error statistics based on the differences among subsamples. Our total trial duration was six years, beginning January 1978 and ending with December 1983. Since the model was initialized from rest, we did not

use the first year of our simulations in the calculation of our statistics. This represents approximately the time required for the Kelvin wave to cross the basin and the reflected Rossby wave to return. A one-year spinup period is also consistent with our calculations of the evolution of the forecast error covariance. This left three possible three year subsamples from five years remaining. We did not use smaller subsamples because the test period contains the intense ENSO event of 1982–83, resulting in a broad scatter in one- or two-year statistics due to the event itself, the setup and the recovery.

Except at Santa Cruz, the variances of the forecast errors differ widely among the subsamples, varying by as much as two to one. Based on this, we had little confidence in the variance pattern itself as a stable estimate of the true ensemble variance. We therefore chose another criterion to fit the parameters of our wind error model.

Upon calculating the error correlation matrix, we found that the two leading EOFs, which together contained more than two-thirds of the total variance, displayed a pattern which appeared in all of the subsamples as well as the overall run. Based on these apparently reliable statistics, we chose to minimize:

$$M = \lambda_1 |\hat{\mathbf{v}}_1 - \tilde{\mathbf{v}}_1|^2 + \lambda_2 |\hat{\mathbf{v}}_2 - \tilde{\mathbf{v}}_2|^2,$$

where λ_1, λ_2 are the lead eigenvalues of the observed error correlation matrix, $\mathbf{v}_j$ is the eigenvector of the observed correlation matrix corresponding to λ_j, $\mathbf{v}_j$ is the corresponding eigenvector of the error correlation predicted by the model. The numerical results of our parameter sweep are shown in Table 1. While the spread in values of M was not extremely large for our range of parameter choices, there was enough sensitivity to distinguish extremes. Since the total variance A enters linearly into the error model and the dynamical model, it enters simply as a variance scale and does not affect the principal components of the error correlation matrix. Here A is fit for given L_x and L_y by applying least squares to the variances for the full 5 year run. While the fits are uncertain, it is worth noting that the values obtained for the parameters of our error models are consistent with our ideas about the errors in the model and in the forcing. The best agreement is obtained with a zonal error correlation scale of 10° and a meridional correlation scale of 2°. Since 2° is the resolution of the wind grid, we cannot distinguish resolutions finer than that. We can, however, perform a calculation in which wind errors at points 2° in latitude apart are independent. This is the case we refer to as $L_y < 2°$. As expected from our analysis in the previous section, the values were more sensitive to the meridional scale than to the zonal. We found the best fit total wind stress error variance A to be $(\rho_a/\rho_w)^2 C_D^2 \times 579\ (\mathrm{m^2\ s^{-2}})^2$, which corresponds to a wind error of roughly 2 m s^{-1}, a figure consistent with the estimates cited in section 2. In summary, a plausible if crude model for the wind stress errors is able to account for the gross characteristics of the model hindcast error, consistent with the assumption that the wind error is the dominant source of system noise.

TABLE 1. Fit of error model parameters to statistics of observed − predicted sea level height anomalies. Values are: $\lambda_1|\hat{\mathbf{v}}_1 - \tilde{\mathbf{v}}_1|^2 + \lambda_2|\hat{\mathbf{v}}_2 - \tilde{\mathbf{v}}_2|^2$.

	L_x			
L_y	5°	10°	20°	30°
<2°	0.7915	0.5892	0.7465	
2°	0.7756	0.5616	0.7518	0.8414
3°		0.5631	0.7393	0.8431
4°		0.5831		

8. Results of filter experiments

a. Comparisons of model output with data at selected stations

The wind error model parameters determined by the process described above were incorporated into the Kalman filter for our model. In this section we present the results of the filter runs, including error estimates. We attempt to verify their accuracy, but the tide gauge network is too sparse to allow definitive verification of the calculation.

A good test of the Kalman filter would be an experiment in which some of the data were withheld from assimilation for comparison purposes. Unfortunately, the sparse and uneven distribution of tide gauge data makes such experiments difficult to interpret. If we were to withhold data from, say, Jarvis Island and use data from Christmas Island for assimilation, the meaning of the results would be unclear. The two are so close that the data at Christmas already contain most of the information from the data at Jarvis: the sample errors at the two stations have a correlation coefficient ≈ 0.9. On the other hand, were we to withhold data at both Jarvis and Christmas, we would anticipate comparatively little impact of the assimilation of data at the other four stations upon those two, because the nearest assimilation point would be Nauru, 33° away. This distance is larger than the wind error correlation scale, so even if the wave amplitudes were known exactly at Nauru, wind errors between Nauru and Jarvis would contribute significantly to the result at Jarvis. No updating scheme, no matter how carefully optimized, can be expected to counteract the effect of this wind error entirely.

While there are not suitable data for thorough quantitative verification of the assimilation model, there are two partial verification methods available: comparison to other stations which were not included, for one reason or another, in the original six, and examination of

TABLE 2. Statistical summary of comutational results.

Station	Observed Variance (cm^2)	Unfiltered Variance (cm^2)				Filtered Variance (cm^2)			
	Total	Total	Error	Est. error	Correlation	Total	Error	Est. error	Correlation
Rabaul	72	57	51	89	.63	76	1	6	1.0
Nauru	118	33	54	30	.76	82	3	6	.99
Jarvis	68	31	27	31	.78	53	3	4	.98
Christmas	100	23	51	37	.73	65	2	5	1.0
Santa Cruz	119	59	61	42	.71	59	4	6	.99
Callao	73	56	52	69	.63	59	1	7	.99
Kapingamarangi	35	33	29	34	.50	88	29	15	.82
Tarawa	78	35	25	35	.83	72	13	10	.93
Canton	55	22	42	51	.53	48	37	30	.73
Fanning	65	19	59	66	.37	73	17	37	.90

the statistical error estimates generated by the filter for consistency. A statistical summary of the results of the runs with updating at six stations appears in Table 2. The comparisons of the observed, filtered and unfiltered results for these six islands are shown in Fig. 3. As expected, the filtered sea levels are almost identical to the observed. This shows the filter to be implemented correctly, but little else.

Four additional stations, Kapingamarangi, Tarawa, Fanning and Canton, are close to the equator and have some data available for the 1978–83 interval, but were not used to update the analysis. The data at Kapingamarangi and Tarawa consist of short, gappy records. The record at Kapingamarangi contains only two April records and three March records. The record at Tarawa is short and is missing most of 1982. This leads to problems of defining means and anomalies, and renders the results problematical. Fanning and Canton are in the Line Islands, very close to Jarvis and Christmas, and cannot be expected to provide much independent information.

The comparisons of observed, filtered and unfiltered results are shown in Fig. 4. The most improvement is at Fanning. This is near Christmas and Jarvis, and benefits from assimilation of data from those nearby stations.

The unfiltered results at Tarawa are good, and assimilation improves them. Tarawa is close to the equator and reasonably far from the western boundary.

The unfiltered results at Canton are very poor. The filtered results are slightly better, but the agreement is still not good.

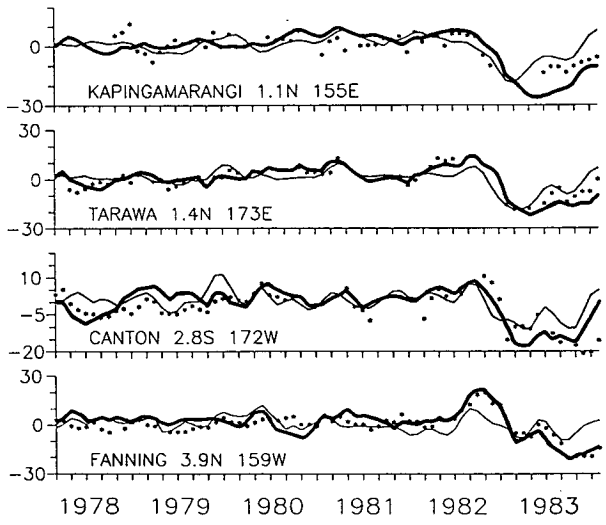

FIG. 4. Comparison of observation, raw model output and filtered output at four stations. Data from these stations did not participate in the assimilation; Observed data points are marked with *; thin line: raw model output; heavy line: filtered model output.

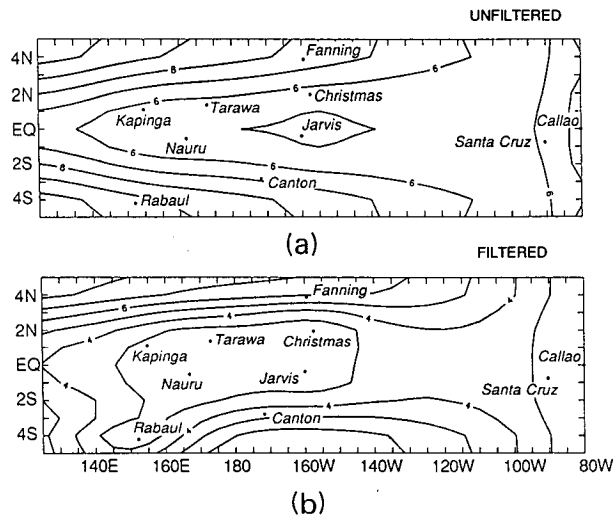

FIG. 5. Contour maps of expected rms error, showing updating and verification sites. (a) expected rms error of raw model output. (b) expected rms error of model updated at the six stations shown in Fig. 1.

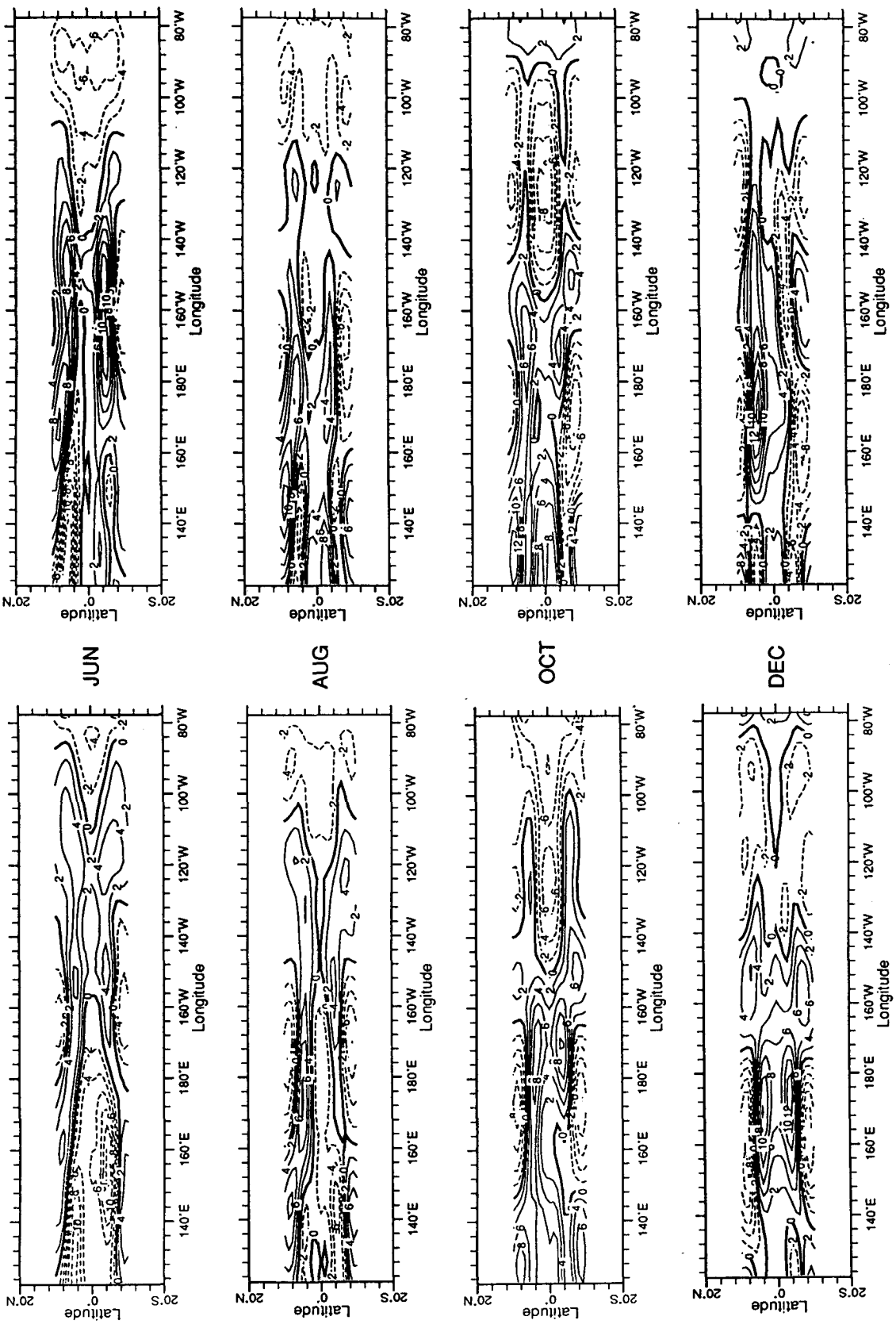

FIG. 6. Contour maps of sea level height from June 1979 to August 1980, showing comparison of raw model output with updated model output.

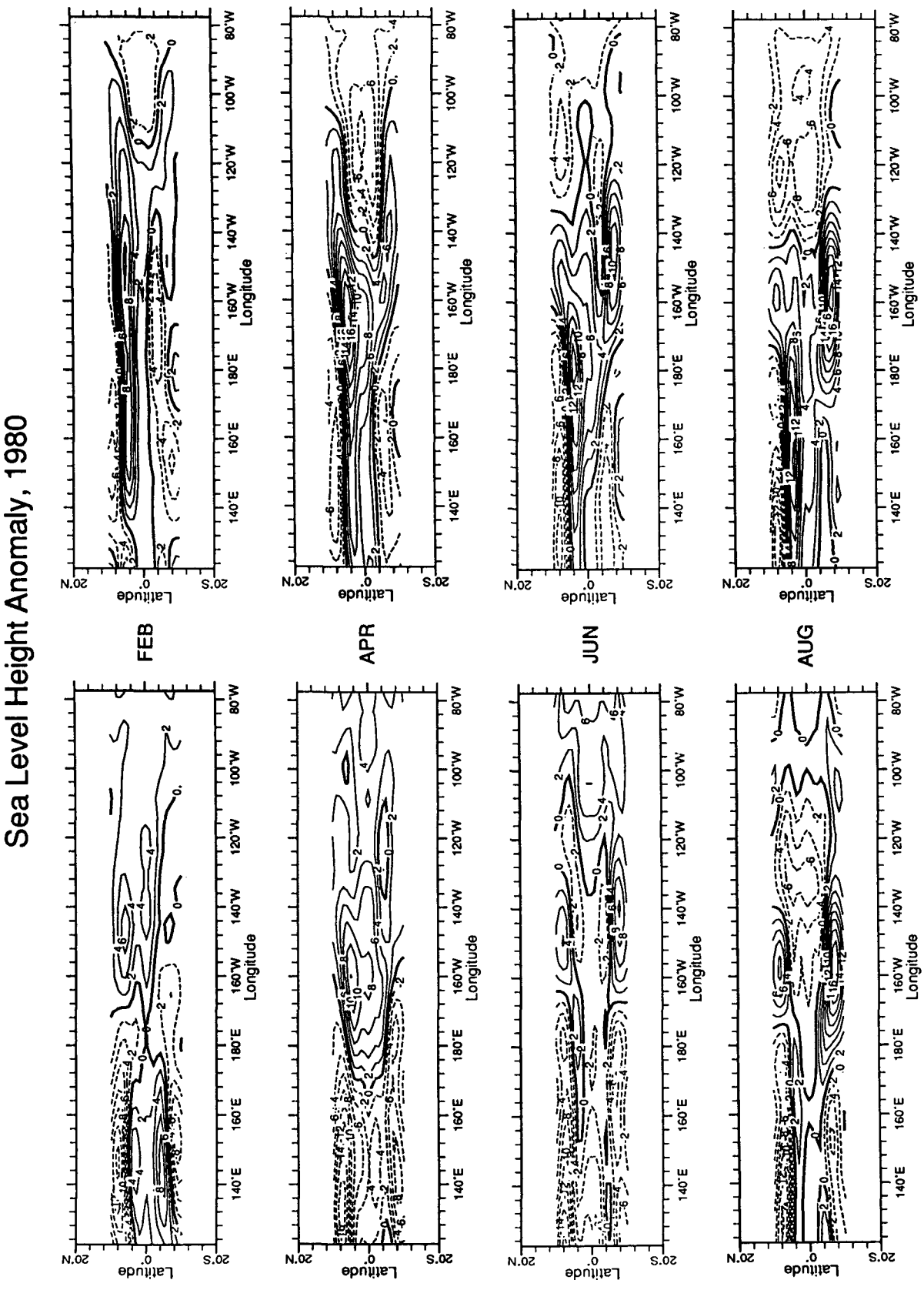

FIG. 6. (*Continued*)

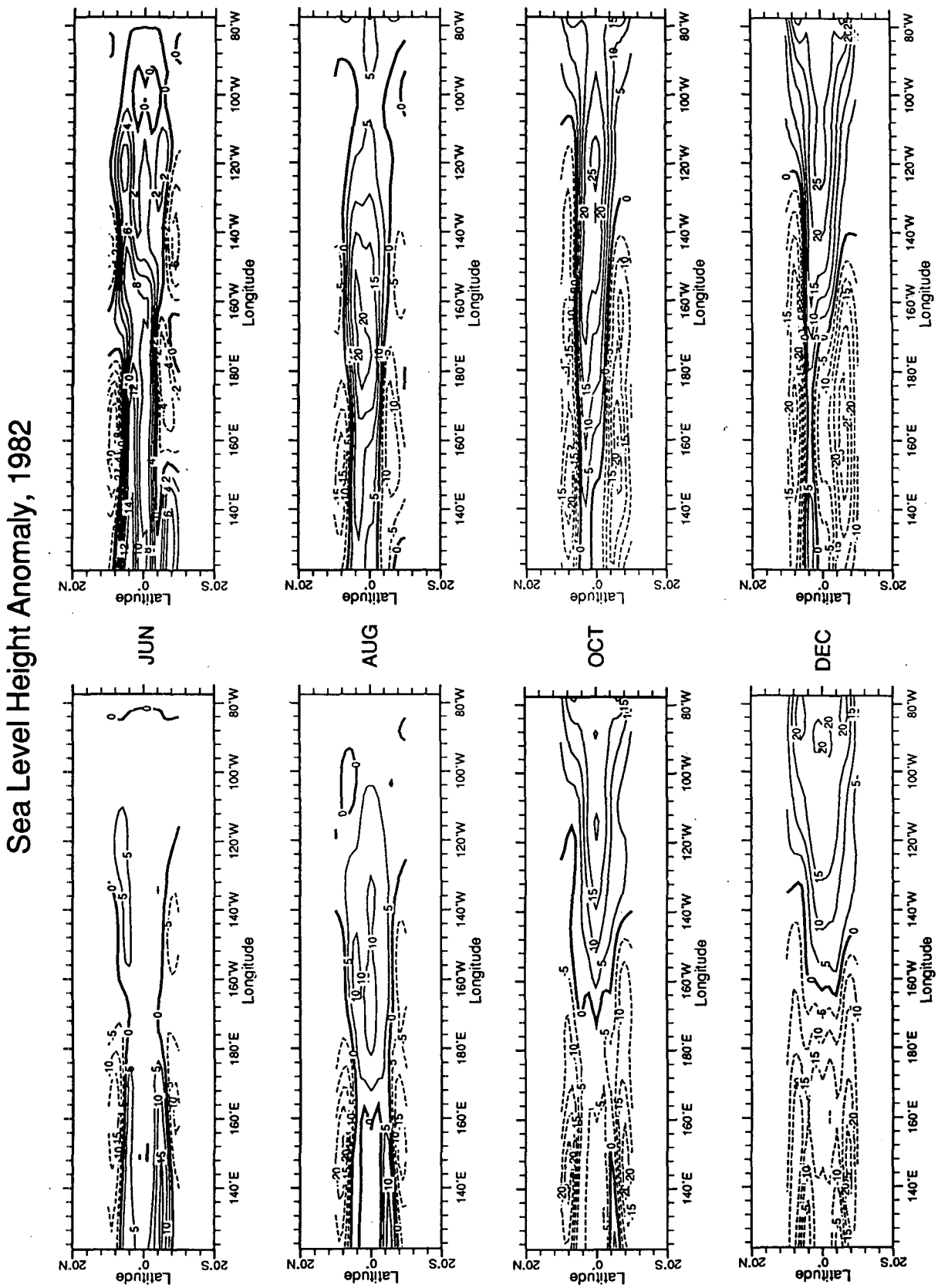

FIG. 7. Contour maps of sea level, similar to Fig. 6, for the strong ENSO event of 1982/83.

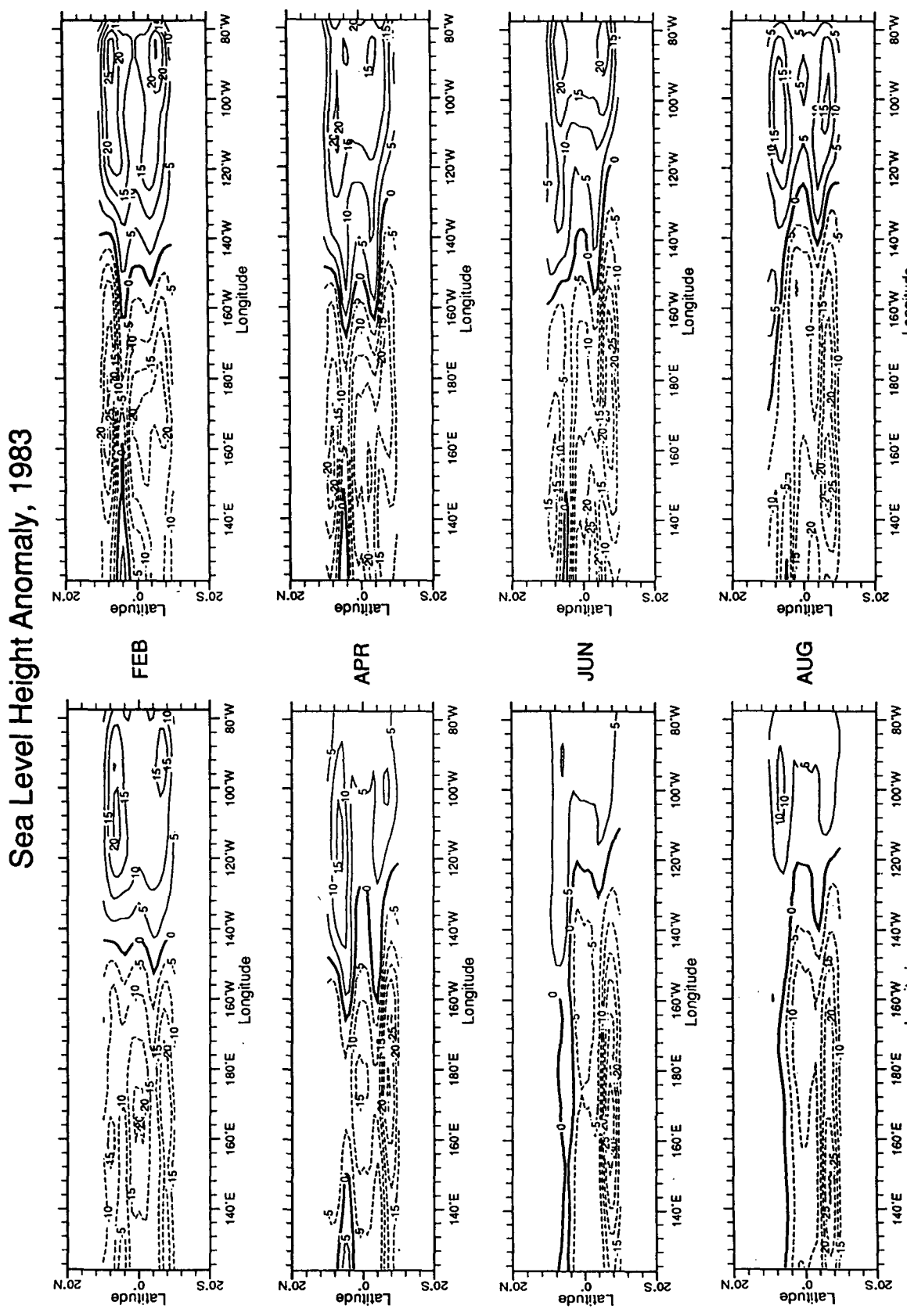

FIG. 7. (*Continued*)

The filter has little effect at Kapingamarangi. Several reasons for this can be suggested. This is the shortest and gappiest of the records. The means and anomalies are therefore most suspect.

It is also close to the western boundary, being almost due north of Rabaul, and may be subject to effects of local geometry. Alternatively, Rabaul may be a poor choice for a data assimilation site for that same reason: note that New Guinea does not appear at all in our model domain, so local effects in the data will not be present in the model and the effects of wind forcing on the model results for that region actually occupied by New Guinea are unpredictable. Finally, the record has a gap during the large ENSO event. At stations where significant improvement is noted, that improvement is largest for the event. This improvement accounts for much of the total improvement in the filtered records.

We can also examine error estimates derived from the output of the filter itself. Figure 5 shows contour maps of the rms expected sea level height error for the unfiltered and filtered cases. The map of the unfiltered error shows a strong meridional gradient approximately 3° from the equator. Verification points at Fanning and Canton islands appear in that band of strong meridional gradient. Poleward of that region the estimated error falls off. This apparently enhanced accuracy is artificial: the model is invalid in that region due to the truncation of the series (1) and the effect of wind stress curl. Generally the map of expected errors can be said to predict the results of the verification experiments. The differences at the updated stations are smaller than the errors the map would suggest, because they are differences with error contaminated data rather than true sea level.

b. *Monthly maps of sea level anomaly*

Monthly maps of sea level anomaly for the period of the simulation were prepared for the model run with and without updating. In view of the expansion in only a few meridional modes the maps can not be expected to have much validity outside of the region very near the equator.

Figures 6 and 7 show two series of maps, one from June 1979 through August 1980 and the other from June 1982 through August 1983, spanning the intense ENSO event. Beginning in June 1979, the updated maps show the region of negative height anomaly in the east extending rather further westward than in the map without updating. The updated map also shows the negative anomalies in the western part of the region restricted to be north of the equator, while the map without updating shows a broad region of negative anomaly. In October, both maps show a broad region of negative height anomaly along the equator centered at about 125°W. By December, this region of negative height anomaly has disappeared to a large extent. Traces remain in the unfiltered map, but the filtered map now has a region of near zero anomaly from 120°W to the eastern boundary.

In February and April of 1980, the filtered maps exhibit long slender regions of positive height anomaly which do not appear quite so distinctly in the unfiltered maps.

In August of 1980, both maps exhibit a region of intense positive height anomaly in the south-central part of the map; the filtered map, however, exhibits a region of strong positive anomaly in the west just north of the equator which does not appear at all in the unfiltered map.

The impact of data assimilation upon the analysis of the intense ENSO event of 1982 is particularly striking. In June of 1982, the filtered map shows very strong positive anomalies in the west along the equator. The anomalies appear only as narrow bands just north and south of the equator in the unfiltered map, and they do not extend past the dateline. By August, the filtered map shows the anomaly on the equator at the dateline to be 20 cm, while it is approximately half that in the unfiltered case. By December, the intense positive anomaly appears in the eastern part of the basin in both maps, but the filtered map shows the anomaly to be stronger, narrower, and greater in extent. It is particularly important to note here that the region from 160° to 90°W is completely data void. The error maps of Fig. 5, which were verified at the four withheld stations, indicate that the differences introduced by the filter represent an improvement.

In 1983, as in the other maps, we observe the features in the filtered maps to be of larger amplitude and to contain more fine structure than the unfiltered maps. By August, the maps are similar west of 120°W or so. In the east, the filtered maps again exhibit more detailed structure, including a region of strong positive anomaly south of the equator and east of 120°W which does not appear in the unfiltered map.

c. *The spatial patterns of the influence of the data*

Another way to study the behavior of the filter is to examine the columns of the gain matrix $\mathbf{K}$. The i, j element of $\mathbf{K}$ can be viewed as the influence of observation j upon state variable i. In our physical model, the state variables are Kelvin and Rossby wave amplitudes. Physical variables such as sea level heights can be calculated as linear functions of the state variables. Thus we may write

$$\tilde{\mathbf{H}}\mathbf{w}_k^a = \tilde{\mathbf{H}}\mathbf{w}_k^f + \tilde{\mathbf{H}}\mathbf{K}_k(\mathbf{w}_k^0 - \mathbf{H}_k\mathbf{w}_k^f),$$

where $\tilde{\mathbf{H}}$ is the matrix which transforms the state vector into a gridded field of sea level anomalies. The columns of $\tilde{\mathbf{H}}\mathbf{K}$ are depicted as spatial maps in Fig. 8 for $\mathbf{K}$ evaluated at the end of the six-year filter run. Places where the mapped function is largest for a given tide gauge station are the places where data from that station have the greatest impact on the analysis.

Often the maximum influence is not located at the station itself. This is a consequence of the inhomogeneity of the observing pattern. Ghil et al. (1981) found a similar result. The maximum influence of the data from Jarvis (Fig. 8c) is south of Jarvis itself. Christmas is sufficiently close to Jarvis that the scheme splits the difference between the two to form the analysis for Jarvis. A few degrees south of Jarvis, the influence of Christmas is weaker, so the data from Jarvis dominate the analysis. The peak influence of the station at Christmas occurs north of the island itself for the same reason.

The influence of Santa Cruz (Fig. 8e) extends much further west than that of Callao (Fig. 8f), which is mostly confined to the coast. The influence of Callao does not diminish significantly in the meridional direction. This follows from the physical approximation in the model that the sea level height is constant along the eastern boundary.

The data from Santa Cruz contribute most strongly to the analysis in the large data void region between the Galapagos and the Line Islands, but no station has much direct influence at 120°W. Consequently, the changes in the structure of the maps there (Figs. 6 and 7) must be attributed to propagation of information from relatively data rich regions.

These maps contain the precise information needed to construct an optimal interpolation (OI) scheme similar to those used in operational numerical weather prediction (e.g., see Lorenc 1986). An OI scheme based on these maps could even be used with a different model such as that of Cane and Patton (1984). Most OI schemes use a specified form of $\tilde{\mathbf{HK}}$, assuming, for example, that the error correlations are homogeneous and isotropic. One could fit a functional form to Fig. 8 without much difficulty. The maps in Fig. 8 are highly anisotropic, but a homogeneous function might not be too bad for stations far from boundaries.

9. Discussion

We have applied a Kalman filter to a simple numerical model driven by analyzed fields of tropical Pacific winds in order to assimilate monthly mean sea level anomalies derived from tide gauge measurements. The maps produced by the Kalman filter, which combines data from the tide gauge network with model output, shows much richer spatial structure than maps derived from the model or data alone. Updating at a mere six stations enriches the structure of the sea level fields considerably. Significantly, the pattern is altered away from the data gathering sites, especially in the data void from the Galapagos to the Line Islands. According to the error estimates, these changes represent an improvement (see Fig. 5): the unfiltered error, which is more than 5 cm almost everywhere, is reduced by 1 cm or more within about 5 degrees of the equator. Since these error estimates are dependent on our error model assumptions, they must be interpreted cautiously. In their support, the a posteriori errors calculated at the few available verification points are consistent with the estimated error (see Table 2).

On the one hand, the improvement is quantitatively small. On the other, it is an impressive change to

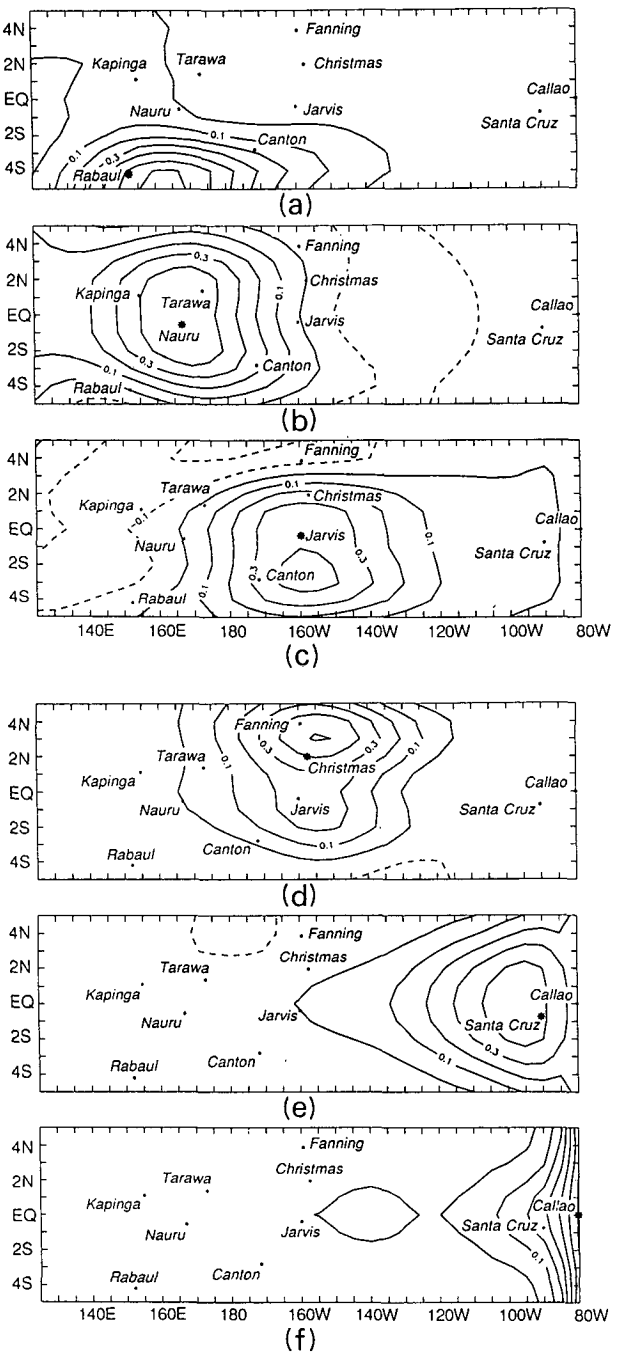

FIG. 8. Contour maps of influence of data at tide gauge stations. The map location of the selected tide gauge station is highlighted. Dashed lines represent negative values. (a) Rabaul, (b) Nauru, (c) Jarvis, (d) Christmas, (e) Santa Cruz, (f) Callao.

squeeze out of only six data points. We can reasonably conclude that the Kalman filter worked, in the sense of making good (and perhaps optimal) use of available data. Nonetheless, it is not the modelers' version of the philosopher's stone, able to turn small quantities of tide and wind data into oceanographer's gold. The need to reproduce reality limits the creativity of any data assimilation scheme; a definitive description of the state of the ocean is impossible without more data.

Though the filter is not miraculous, it is an instrument with many virtues. Given the general rule that the utility of data is enhanced by error bars, the error maps are a valuable adjunct to the filtered model results. Within the limits imposed by our uncertain knowledge of the model and data errors, the Kalman filter, being optimal, tells us the best we can hope to do with the available data. Proposed changes in the observing system can readily be evaluated by applying the filter formalism in simulation studies. The error maps are an immediate indication of their potential.

In order to implement the Kalman filter, we had to form an estimate of the covariance of the error in the *model.* We derived this estimate by assuming that all of the error in the model output resulted from errors in the pseudostress fields used to drive the model. The parameters fitted to the statistics of the actual differences between the data and the model output were consistent with generally accepted estimates of the actual error in the pseudostress field. It might seem to some that a model as crude as the one used here would contain physical errors that would be comparable in magnitude to those resulting from errors in the wind. If this is the case, quantitative estimates of the effects of such errors are lacking. Neither nonlinearities nor errors in the wave speed, for example, could be expected to contribute nearly as much to the error amplitude as wind errors of the magnitude we expect. The question of how large the errors would be if we had perfect winds cannot be answered by our analysis here.

We have calculated the level of the system noise necessary to explain all of the difference between our model calculation and the data. If we interpret this system noise as being entirely due to error in the wind field, we then find these errors in the wind field to be consistent in magnitude and covariance characteristics with prevailing estimates of the statistics of the wind field error. This is the precise statement of our result.

We expect two types of experiments, in particular, to shed light on the future direction of this work. One is obviously the use of different types of data such as satellite altimetry or hydrographic data. The other is a series of observing system simulation experiments, in which appropriate random perturbations added to the wind field, and sea level heights from the unperturbed model run are assimilated into predictions made using the perturbed winds.

Acknowledgment. This work was supported by the National Science Foundation Grant OCE86-11434, NOAA Grant NA-87-AA-D-ACO81 and JPL Grant JPL 957647. We would also like to thank Michael Ghil for his part in giving this project its initial shove and for helpful discussions along the way.

REFERENCES

Cane, M. A., 1984: Modeling sea level during El Niño. *J. Phys. Oceanogr.*, **14,** 1864–1874.

——, 1986: El Niño. *Ann. Rev. Earth Planet. Sci.*, **14,** 43–70.

——, and E. S. Sarachik, 1981: The response of a linear baroclinic equatorial ocean to periodic forcing. *J. Mar. Res.*, **39,** 651–693.

——, and R. J. Patton, 1984: A numerical model for low-frequency equatorial dynamics. *J. Phys. Oceanogr.*, **14,** 1853–1863.

——, S. E. Zebiak and S. C. Dolan, 1986: Experimental forecasts of El Niño. *Nature,* **322,** 827–832.

Chelton, D. B., and J. J. O'Brien, 1982: Satellite microwave measurements of surface wind speed in the tropical Pacific. *Trop. Ocean-Atmos. Newslett.*, **11,** 2–4.

Cheney, R. L., L. L. Miller, B. C. Douglas and R. W. Agreen, 1987: Monitoring equatorial Pacific sea level with Geosat. Johns Hopkins APL Technical Digest No. 8, 245–250.

Dee, D. P., S. E. Cohn and M. Ghil, 1985: An efficient algorithm for estimating noise covariance in distributed systems. *IEEE Trans. Autom. Control,* **AC-30,** 1057–1065.

Ghil, M., S. E. Cohn, J. Tavantzis, K. Bube and E. Isaacson, 1981: Applications of estimation theory to numerical weather prediction. *Dynamic Meteorology: Data Assimilation Methods,* L. Bengtsson, M. Ghil and E. Kallen, Eds., Appl. Math. Sci. Ser. Vol. 36, Springer-Verlag, 330 pp.

Gill, A. E., 1983: An estimation of sea-level and surface-current anomalies during the 1972 El Niño and consequent thermal effects. *J. Phys. Oceanogr.*, **13,** 586–606.

Goldenberg, S. B., and J. J. O'Brien, 1981: Time and space variability of tropical Pacific wind stress. *Mon. Wea. Rev.*, **109,** 1190–1207.

Halpern, D., and D. E. Harrison, 1982: Intercomparison of tropical Pacific mean November 1979 surface wind fields. Report 82-1, Department of Meteorology and Physical Oceanography, Massachusetts Institute of Technology, 40 pp.

Latif, M., 1987: Tropical ocean circulation experiments. *J. Phys. Oceanogr.*, **17,** 246–263.

Leetmaa, A., and M. Ji, 1989: Operational hindcasting of the tropical Pacific. *Dyn. Atmos. Oceans,* in press.

Lorenc, A. C., 1986: Analysis methods for numerical weather prediction. *Quart. J. Roy. Meteor. Soc.*, **112,** 1177–1194.

McPhaden, M. J., A. J. Busalacchi and J. Picaut, 1988: Observations and wind-forced simulations of the mean seasonal cycle in tropical Pacific sea surface topography. *J. Geophys. Res.*, **93,** 8131–8146.

Miller, R. N., 1986: Toward the application of the Kalman filter to regional open ocean modeling. *J. Phys. Oceanogr.*, **16,** 72–86.

Sasaki, Y., 1970: Some basic formalisms in numerical variational analysis. *Mon. Wea. Rev.*, **98,** 875–833.

White, W. B., S. Pazan and M. Inoue, 1987: Hindcast/forecast of ENSO events based upon the redistribution of observed and model heat content in the western tropical Pacific, 1964–86. *J. Phys. Oceanogr.*, **17,** 264–280.

Wyrtki, K., 1975: El Niño: the dynamic response of the equatorial Pacific Ocean to atmospheric forcing. *J. Phys. Oceanogr.*, **5,** 572–584.

——, 1979: The response of sea surface topography to the 1976 El Niño. *J. Phys. Oceanogr.*, **9,** 1223–1231.

——, and S. Nakahara, 1984: Monthly maps of sea level anomalies in the Pacific, 1975–1981. Technical report HIG-84-3, Hawaii Institute of Geophysics, Honolulu, Hawaii. 93 pp.

——, K. Constantine, B. J. Kilonsky, G. Mitchum, B. Miyamoto, T. Murphy, S. Nakahara and P. Caldwell, 1988: The Pacific Island Sea Level Network. JIMAR Contribution No. 88-0137, Data report No. 002, Joint Institute for Marine and Atmospheric Research, University of Hawaii, Honolulu, Hawaii, 71 pp.